Electronic Supplementary Information (ESI)

Synthesis of plasmonic Fe/Al nanoparticles in ionic liquids

Alexa Schmitz,[a] Hajo Meyer,[b] Michael Meischein,[b] Alba Garzón Manjón,[c] Laura Schmolke,[a] Beatriz Giesen,[a] Carsten Schlüsener,[a] Paul Simon,[d] Yuri Grin,[d] Roland A. Fischer,[e] Christina Scheu,[c] Alfred Ludwig[b] and Christoph Janiak[a,*]

1 Institut für Anorganische Chemie und Strukturchemie, Heinrich-Heine-Universität Düsseldorf, D-40204 Düsseldorf, Germany. Fax: +49-211-81-12287; Tel: +49-211-81-12286. E-mail: janiak@uni-duesseldorf.de
2 Materials Discovery and Interfaces, Institut für Werkstoffe, Fakultät für Maschinenbau, Ruhr-Universität Bochum, Universitätsstr.150, D-44801 Bochum, Germany
3 Max-Planck-Institut für Eisenforschung GmbH, Max-Planck-Straße 1, D-40237 Düsseldorf, Germany
4 Max-Planck-Institut für Chemische Physik fester Stoffe, Nöthnitzer Straße 40, D-01187 Dresden, Germany
5 Department of Chemistry, Technische Universität München, D-85748 Garching, Germany

Email addresses: alexa.schmitz@hhu.de, hajo.meyer@hhu.de, michael.meischein@rub.de, a.garzon@mpie.de, laura.schmolke@hhu.de, beatriz.giesen@hhu.de, carsten.schluesener@hhu.de, paul.simon@cpfs.mpg.de, juri.grin@cpfs.mpg.de, roland.fischer@tum.de, c.scheu@mpie.de, alfred.ludwig@rub.de

Content

Synthesis of ionic liquids

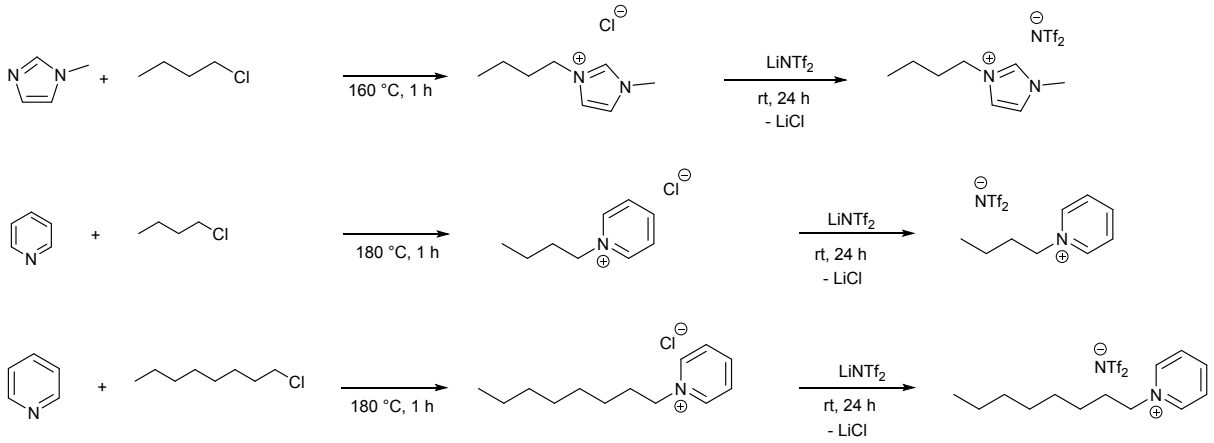

Scheme S1 Synthesis scheme of the three used ionic liquids. Top: 1-butyl-3-methylimidazolium bis(trifluoromethylsulfonyl)imide [BMIm][NTf_2], middle: 1-butylpyridinium bis(trifluoromethylsulfonyl)imide [BPy][NTf_2], bottom: 1-octylpyridinium bis(trifluoromethyl-sulfonyl)imide [OPy][NTf_2].

Device construction for the sputter deposition

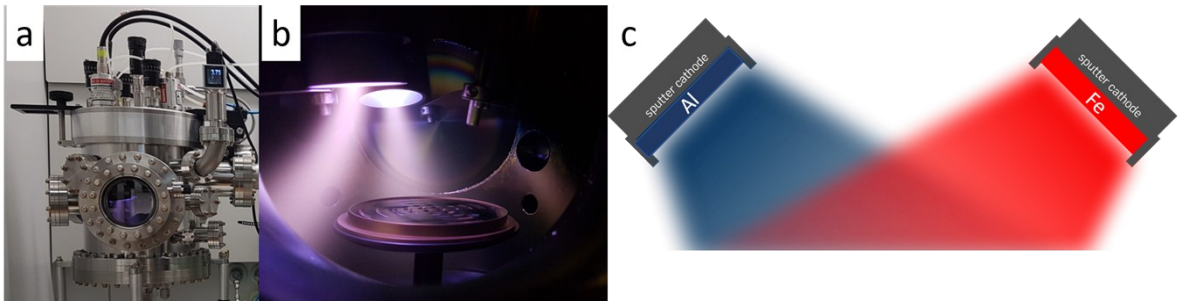

Fig. S1 (a) Sputter chamber from the outside, (b) sputter chamber from the inside, (c) schematic sputter chamber.

Bottom-up synthesis of Fe/Al nanoparticles

Reaction of $FeCl_2$ and $LiAlH_4$ in $[OPy][NTf_2]$

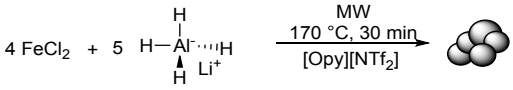

Fig. S2 Synthesis of Fe/Al-NPs from $FeCl_2$ and $LiAlH_4$ by microwave-(MW-)assisted heating in $[OPy][NTf_2]$.

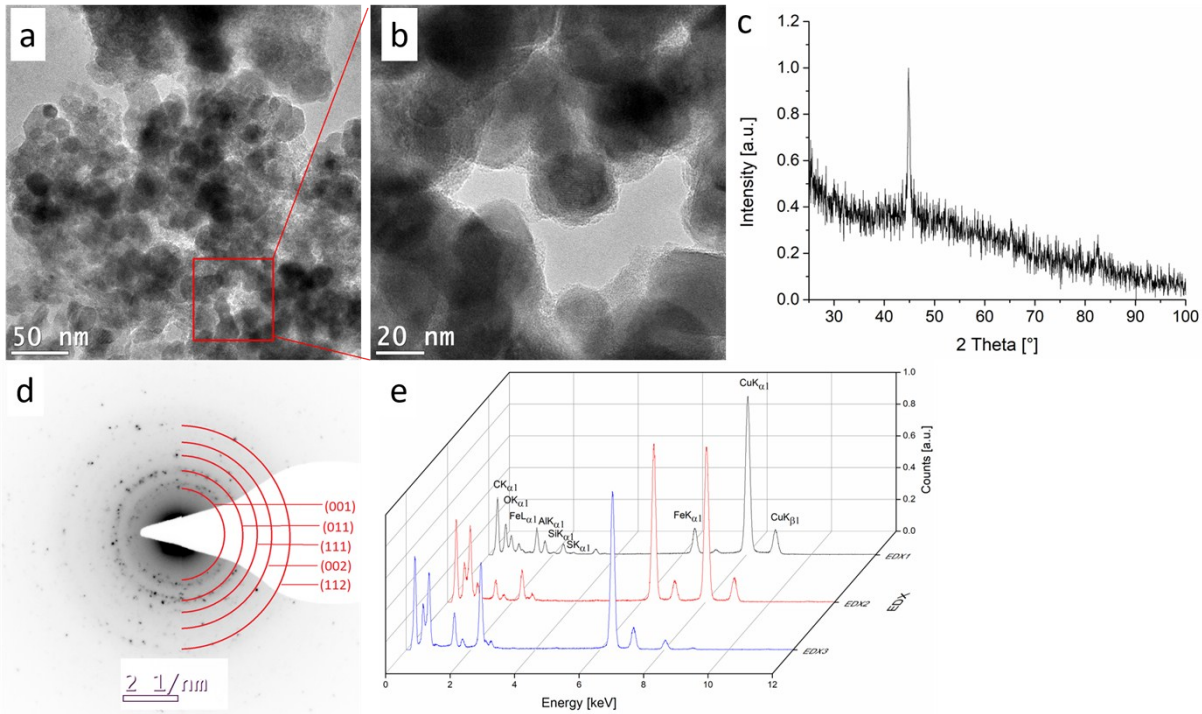

Fig. S3 (a,b) TEM images of the nanoparticles from $FeCl_2$ and $LiAlH_4$ in $[OPy][NTf_2]$. (c) PXRD of the FeAl-NPs from $FeCl_2$ and $LiAlH_4$ in $[OPy][NTf_2]$. (d) SAED of the FeAl-NPs (FeAl reference reflexes in red from COD: 1541193, with cubic space group $Pm\bar{3}m$. (e) EDX spectra of three areas of the sample from the reaction of $FeCl_2$ and $LiAlH_4$ in $[OPy][NTf_2]$.

Reaction of [LiFe(btsa)$_3$] and LiAlH$_4$

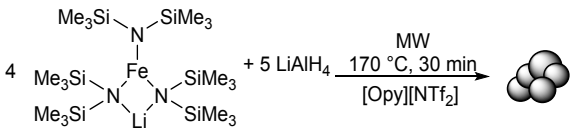

Fig. S4 Synthesis of Fe/Al nanoparticles (NPs) from [LiFe(btsa)$_3$] and LiAlH$_4$ by microwave-assisted heating in [OPy][NTf$_2$].

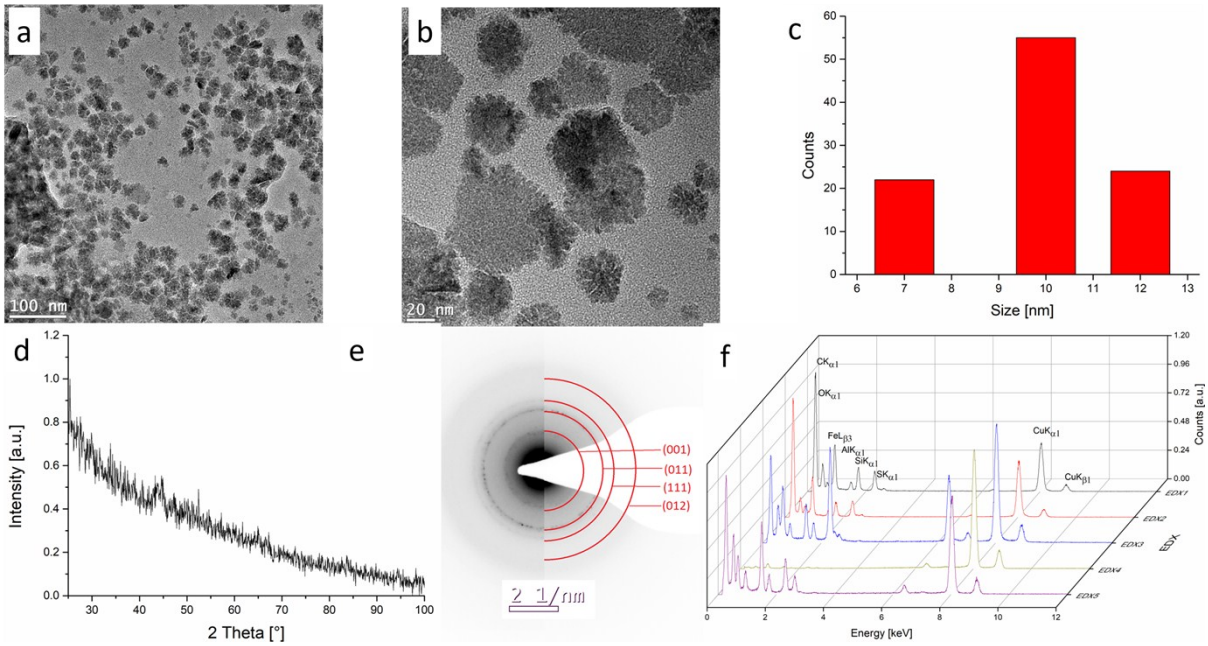

Fig. S5 (a,b) TEM images of 1 wt.-% Fe/Al NPs from [LiFe(btsa)$_3$] and LiAlH$_4$ in [OPy][NTf$_2$], (c) particle size histogram. (d) PXRD of the FeAl-NPs from [LiFe(btsa)$_3$] and LiAlH$_4$ in [OPy][NTf$_2$]. (e) SAED of the FeAl-NPs (FeAl reference reflexes in red from COD: 1541193, with cubic space group $Pm\bar{3}m$. (f) EDX spectra of four areas of the sample from the reaction of [LiFe(btsa)$_3$] and LiAlH$_4$ in [OPy][NTf$_2$].

Decomposition of $Fe(CO)_5$ and $[(AlCp^*)_4]$

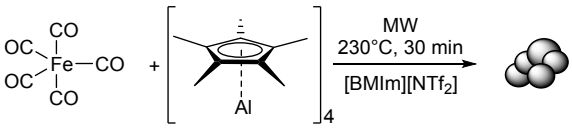

Fig. S6 Synthesis of Fe/Al-NPs from $Fe(CO)_5$ and $[(AlCp^*)_4]$ by microwave-assisted heating in $[BMIm][NTf_2]$.

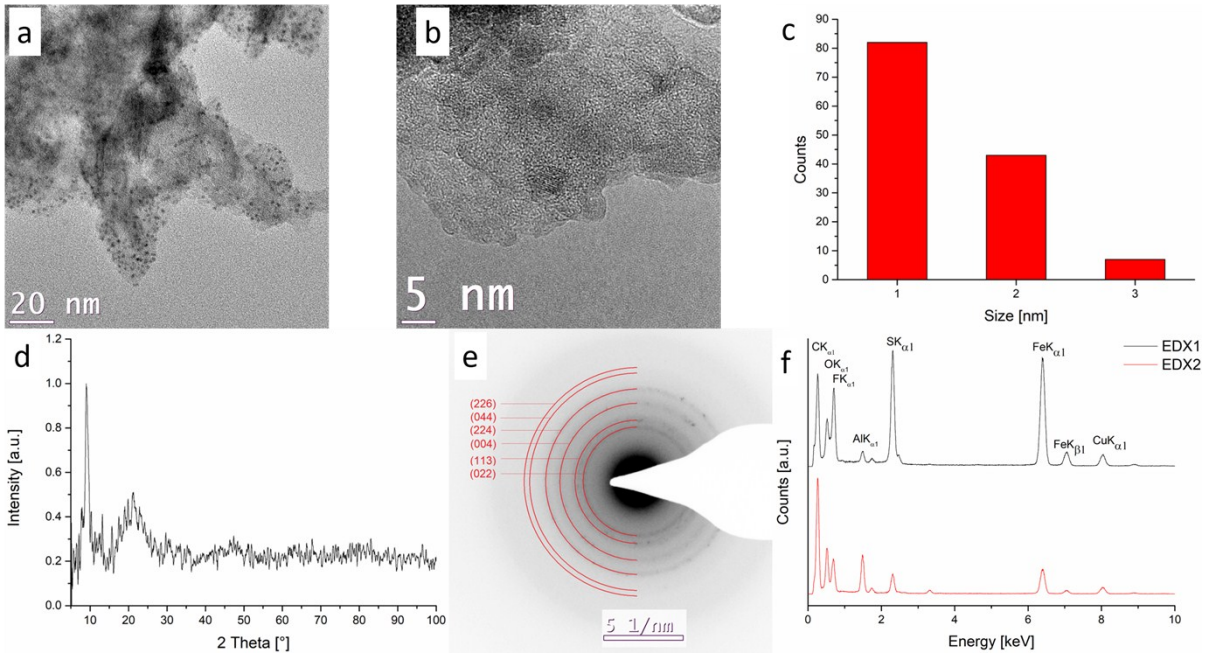

Fig. S7 (a,b) TEM images of 1 wt.-% Fe/Al NPs from $Fe(CO)_5$ and $[(AlCp^*)_4]$ in $[BMim][NTf_2]$. (c) particle size histogram. (d) PXRD of the $FeAl_2O_4$-NPs from $Fe(CO)_5$ and $[(AlCp^*)_4]$ in $[BMIm][NTf_2]$. (e) SAED of the $FeAl_2O_4$-NPs ($FeAl_2O_4$ reference reflexes in red from COD: 9012446) with cubic space group $Fd\bar{3}m$. (f) EDX of the $FeAl_2O_4$-NPs from $Fe(CO)_5$ and $[(AlCp^*)_4]$ in $[BMIm][NTf_2]$.

Reaction of $Fe_2(CO)_9$ and $[(AlCp^*)_4]$

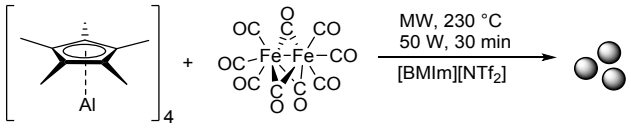

Fig. S8 Attempted synthesis of Fe/Al nanoparticles from $Fe_2(CO)_9$ and $[(AlCp^*)_4]$ by microwave-assisted heating in $[BMIm][NTf_2]$.

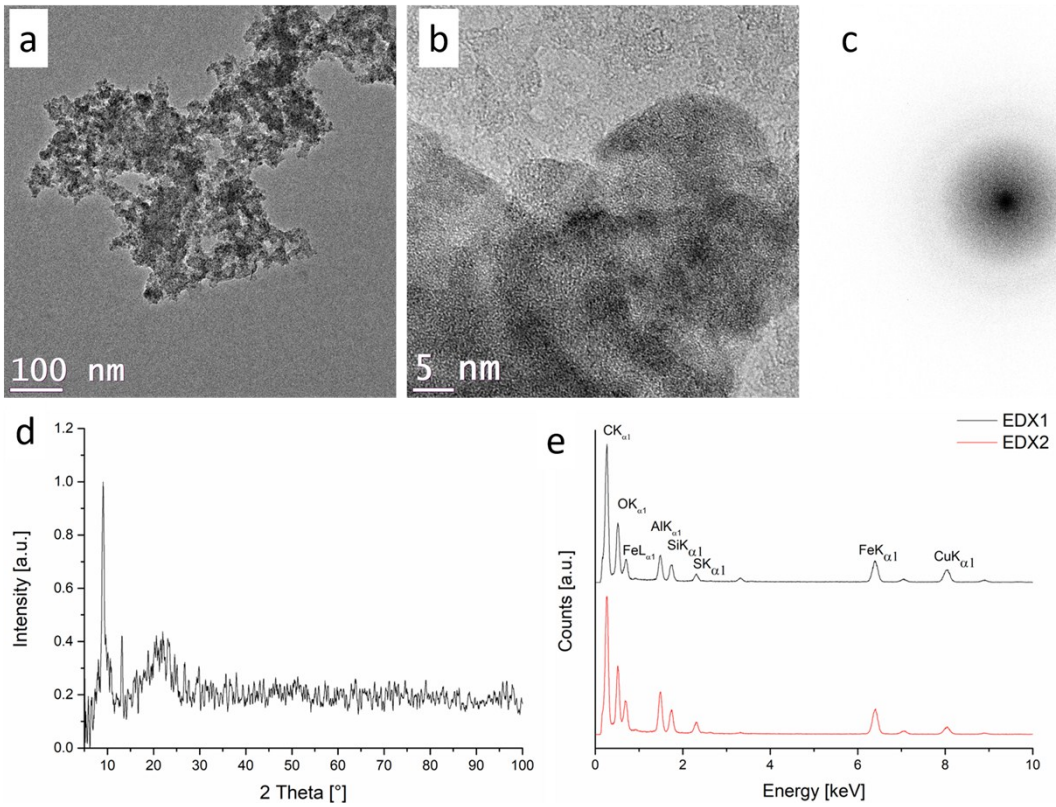

Fig. S9 (a,b)TEM images from the reaction product of $Fe_2(CO)_9$ and $[(AlCp^*)_4]$. (c) FFT of (b). (d) PXRD from the reaction product of $Fe_2(CO)_9$ and $[(AlCp^*)_4]$. (e) EDX from reaction product of $Fe_2(CO)_9$ and $[(AlCp^*)_4]$.

Decomposition of [(CO)$_4$FeAlCp*]

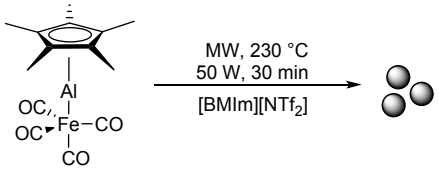

Fig. S10 Attempted synthesis of Fe/Al nanoparticles from [(CO)$_4$FeAlCp*] by microwave-assisted heating in [BMIm][NTf$_2$].

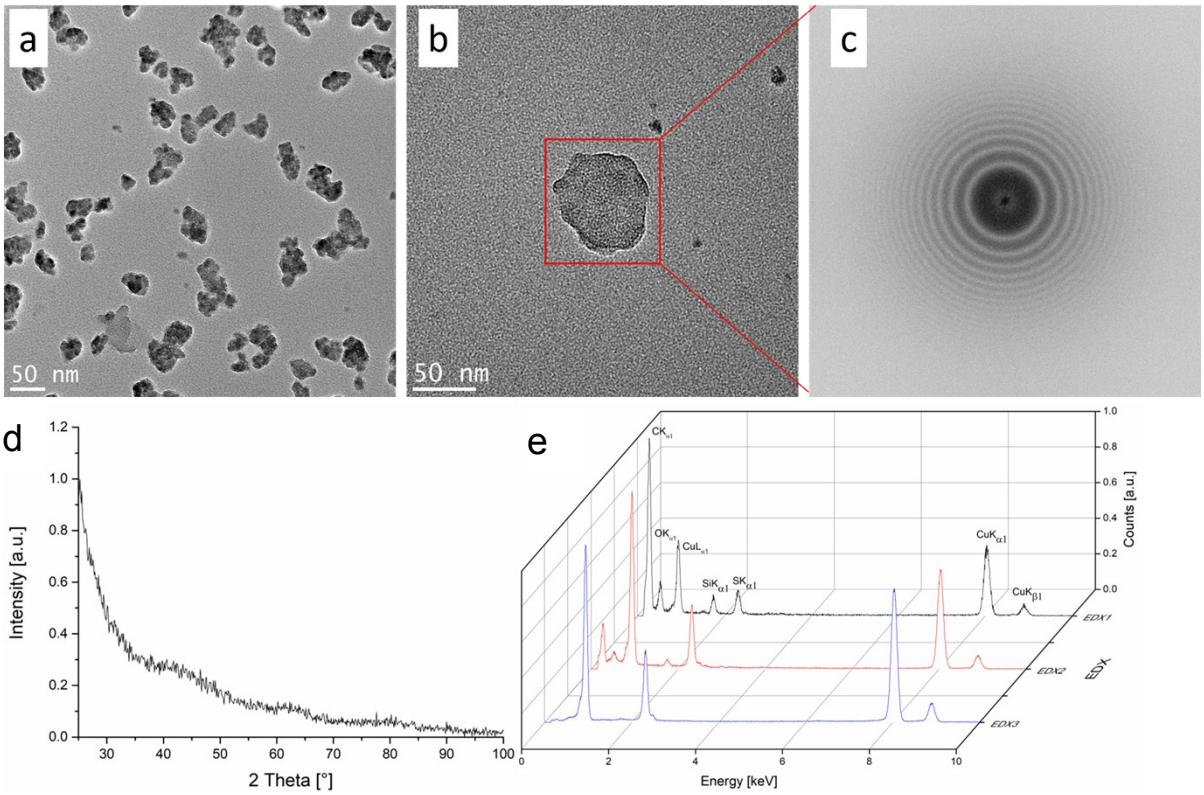

Fig. S11 (a,b) TEM images of the decomposition product of [(CO)$_4$FeAlCp*]. (c) FFT of (b). (d) PXRD of the decomposition product of [(CO)$_4$FeAlCp*]. (e) EDX of the decomposition product of [(CO)$_4$FeAlCp*].

TGA, AAS and SEM/EDX analysis

The three nanoparticle samples from the decomposition of $Fe(CO)_5$, $Fe_2(CO)_9$ and $FeCl_2$ were analyzed by TGA and AAS. The TGA is shown in Fig. S11. For the sample from $Fe(CO)_5$ a mass loss of 60% was found up to 1000 °C, for $Fe_2(CO)_9$ a mass loss of 50% and for $FeCl_2$ a mass loss of 55%.

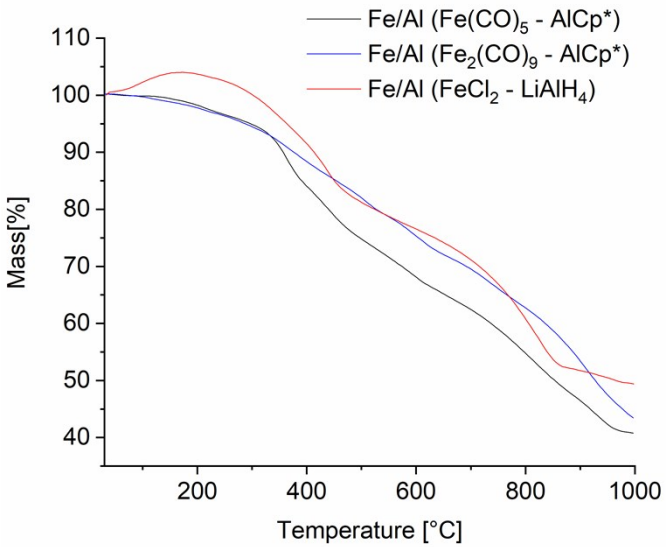

Fig. S12 TGA analysis under nitrogen atmosphere at a heating rate of 5 °C/min. Black curve: Fe/Al NPs from $Fe(CO)_5/(AlCp^*)_4$ in $[BMIm][NTf_2]$. Blue curve: Fe/Al NPs from $Fe_2(CO)_9/(AlCp^*)_4$ in $[BMIm][NTf_2]$. Red curve: Fe/Al NPs from $FeCl_2/LiAlH_4$ in $[OPy][NTf_2]$.

The observed mass loss in the thermogravimetric analysis is assigned to the adhering ionic liquid which could not be removed by the precipitation and washing process.

For the amount of metal, the samples were measured by AAS, namely the precipitated, separated and washed samples from the NP/IL dispersions and the TGA residue. The results are shown in Table S1.

Before discussing the TGA and AAS results we must note that measuring aluminum by AAS proved difficult. The readily available method for Al determination on the Perkin-Elmer PinAAcle 900T was based on using graphite-furnace AAS (GF-AAS). The calibration curve was linear in the region 15-200 µg/L. (Flame-AAS would have required the use of nitrous oxide (N_2O) as oxidant which was not available.)

The AAS instrument construction required a solution also for the graphite-furnace mode, which had to be injected by the automatic sampler. A manual application of the sample into the graphite tube was not possible. Such a manual would have allowed the direct insertion of the solid probe. We note that also ICP-MS or ICP-AES/OES mostly work with solution samples. Solid samples can only be analyzed through ICP when a laser-ablation is available for vaporization.

Table S1 Iron and aluminum AAS results of bottom-up NP/IL samples.[a]

Sample NPs from ...[b]	**Weight sample [mg]**	**Weight Fe [mg]**	**Fe [wt.%]**	**Weight Al [mg]**	**Al [wt.%]**
$FeCl_2$, $LiAlH_4$	4.2	0.4	10(1)	0.9	21(4)
$FeCl_2$, $LiAlH_4$ TGA residue	1.8	0.5	28(3)	0.6	38(8)
$Fe(CO)_5$, $(AlCp^*)_4$	4.9	1.0	20(2)	0.3	6(1)
$Fe(CO)_5$, $(AlCp^*)_4$ TGA residue	1.4	1.2	86(9)	0.2	14(3)
$Fe_2(CO)_9$, $(AlCp^*)_4$	1.3	0.7	54(5)	0.2	15(3)
$Fe_2(CO)_9$, $(AlCp^*)_4$ TGA residue	1.6	0.7	44(4)	0.8	50(10)

[a] A minimum error of 10% for Fe and 20% for Al was assumed based on the weighing accuracy, the sample preparation procedure with dissolution by aqua regia digestion and filtration and for Al the variation in the replicate measurements (see text). The blind values for Fe and Al from the aqua regia had been deducted. [b] The samples were measured as precipitated, separated and washed NP/IL dispersions and as TGA residue. Solutions for AAS were obtained by digesting in hot aqua regia for two times. The residues were re-dissolved in aqua regia (8 mL), filtered and brought with water to a total volume of 50 mL. For the iron measurements the samples were diluted 1:10 and the aluminum 1:100.

GF-AAS is one of only a few routine sensitive techniques to measure Al. Still, the matrix requires special attention and possibly tailored additives in the case of Al according to the Perkin-Elmer application note.

A method for aluminum GF-AAS determination suggested the addition of magnesium nitrate as a modifier to reduce the volatility. Magnesium is a first-class modifier, forming oxides in the graphite furnace during heat pre-treatment.[1] Mg and Al form Mg-Al oxides. Yet, with our samples, also from the TGA residue, a double peak was observed, hence, $Mg(NO_3)_2$ was not added. Furthermore, the addition of $Mg(NO_3)_2$ also decreased the measured Al content in the samples.

When the Al-samples from the same probe were injected three times to replicate the measurement large deviations of about 10% in the concentration values were obtained. For the iron measurements these deviations were only 1%.

In the Perkin-Elmer application note and deposited method for Al determination by GF-AAS a temperature program was given consisting of drying at 120 °C for 1/10 sec (ramp/hold time), drying at 140 °C for 5/10 sec, drying at 200 °C for 5/5 sec, pyrolysis at 1200 °C for 5/15 sec, atomization at 2300 °C for 0/5 sec and clean-out at 2450 °C for 1/3 sec. This temperature program was also modified by variation of drying and pyrolysis time and atomization temperature in order to improve the reproducibility of the replicate measurements and the peak form, with and without modifier.

In summary, for aluminum analyses by GF-AAS the temperature program, matrix and added modifying reagents prove highly crucial. The principle problem with Al determinations by GF-AAS appear to the volatilization as a stable oxide which only partially dissociates if the temperature is too low. Volatilization muss be delayed until the gas phase has reached a higher, steady-state temperature to increase the atomization efficiency. Despite many attempts satisfying Al measurements could not be reached.

The AAS results for the samples from $FeCl_2/LiAlH_4$ and $Fe(CO)_5/(AlCp^*)_4$ can be brought into agreement with the TGA results. These samples had a total (Fe+Al) metal content from AAS below the mass loss seen in TGA. At the same time, the samples of the TGA residues from $Fe(CO)_5/(AlCp^*)_4$ and $Fe_2(CO)_9/(AlCp^*)_4$ showed 100 wt.% total (Fe+Al) metal, in agreement with the quantitative removal of adhering IL up to 1000 °C. For the $FeCl_2/LiAlH_4$ sample of the TGA residue with ~70 wt.% total metal we assume the presence of residual Fe-chloride species.

In view of the apparent problems with the AAS metal determinations we have also analyzed the element content of the three bottom-up samples by SEM-EDX. The EDX-derived content of iron, aluminum and fluoride is given in Table S2.

Table S 2 Content of iron, aluminium and fluoride from SEM-EDX.[a]

Sample NPs from ...[b]	**Fe [%]**	**Al [%]**	**F [%]**
$FeCl_2$, $LiAlH_4$	26	28	46
	17	24	59
	19	30	52
	18	25	57
$Fe(CO)_5$, $(AlCp^*)_4$	67	15	18
	64	13	23
	58	13	29
	63	15	22
$Fe_2(CO)_9$, $(AlCp^*)_4$	47	39	14
	44	39	18
	44	41	15
	44	33	23

[a] The samples were measured as precipitated, separated and washed NP/IL dispersions. The samples also contain C, O, N, S, Au (from sputtering) etc. The at.% values for Fe:Al:F were normalized to 100% for better comparison.

The EDX results showed the same trend in the Fe:Al ratio as the AAS results (cf. Table S1 and S2). There is more aluminum than iron for the sample from $FeCl_2/LiAlH_4$, a higher content of iron for the sample from $Fe(CO)_5/(AlCp^*)_4$ and an about equal Fe:Al ratio for the sample from $Fe_2(CO)_9/(AlCp^*)_4$. Thus, SEM-EDX supports the AAS results. The fluoride content from SEM-EDX shows the adhering IL to the metal nanoparticles.

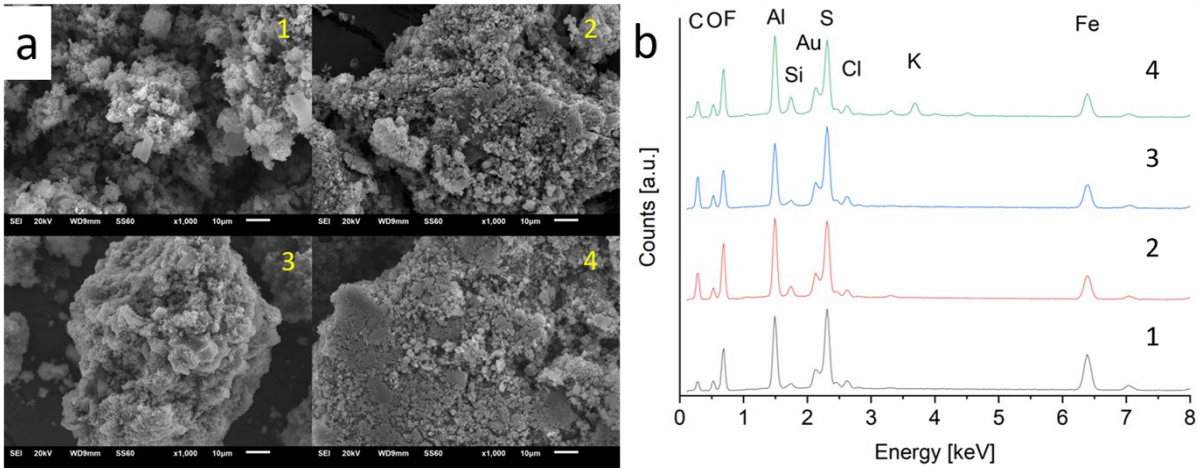

Fig. S13 (a) SEM images for the four EDX spectra and associated (b) EDX spectra for the precipitated, separated and washed NP/IL dispersion from $FeCl_2/LiAlH_4$.

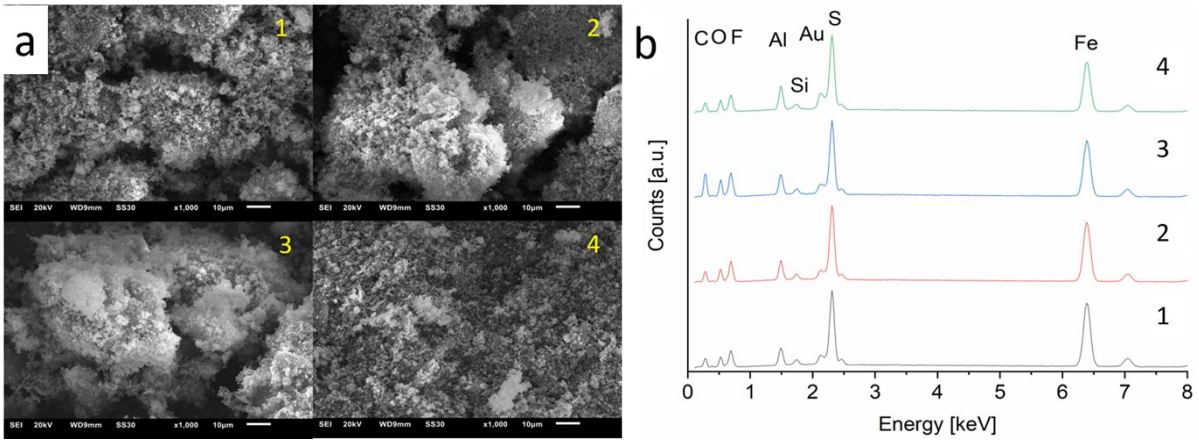

Fig. S14 (a) SEM images for the four EDX spectra and associated (b) EDX spectra for the precipitated, separated and washed NP/IL dispersion from $Fe(CO)_5/(AlCp^*)_4$.

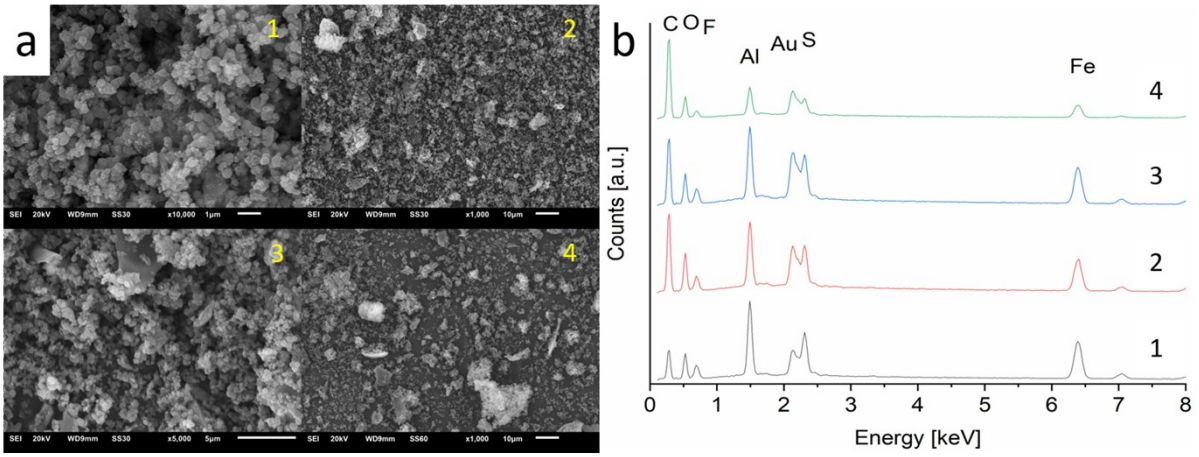

Fig. S15 (a) SEM images for the four EDX spectra and associated (b) EDX spectra for the precipitated, separated and washed NP/IL dispersion from $Fe_2(CO)_9/(AlCp^*)_4$.

Top-down synthesis of Fe/Al nanoparticles by magnetron co-sputtering of Fe and Al into ionic liquids

XPS of the co-sputtered Fe/Al in [OPy][NTf_2]

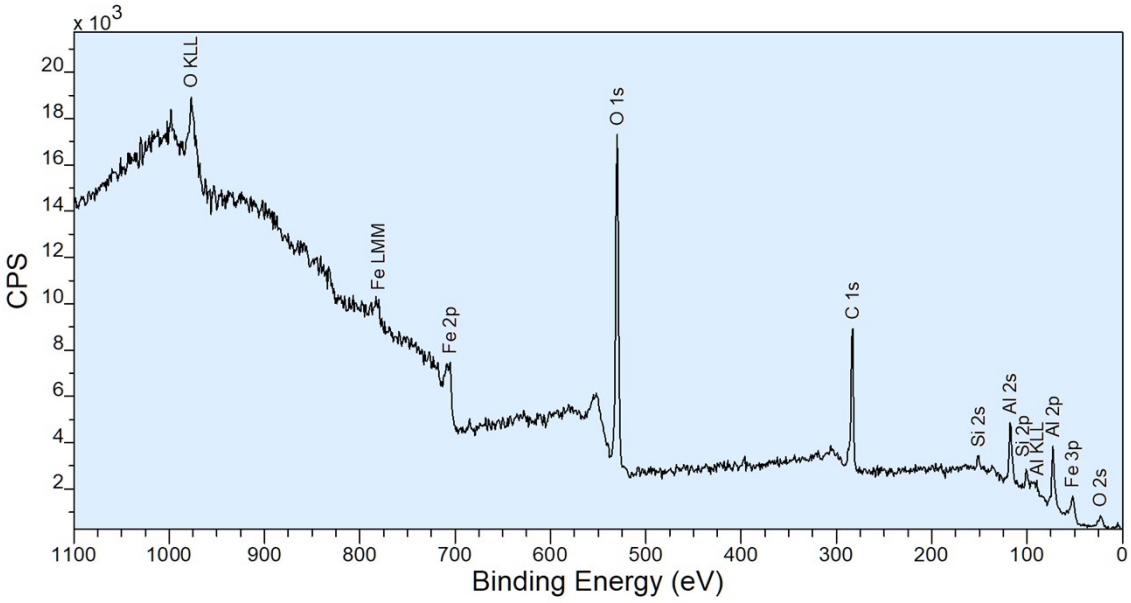

Fig. S16 XPS survey spectrum of the co-sputtered Fe/Al on the silicon wafer.

Table S3 Comparison of XPS binding energies from the co-sputtered Fe/Al wafer.

XPS signal	**Fe/Al wafer**	**References**[2-3]
Al 2p	72.0	Al^0 72.7
[eV]	74.3	Al_2O_3 74.1
Fe 2p $^3/_2$	706.2	Fe^0
[eV]	707.1-710.1	Fe^{II}/Fe^{III}
O 1s	530.7	M-Ox
[eV]	532.0	SiO_2

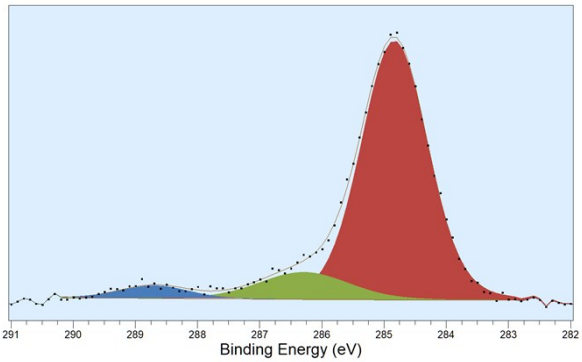

Fig. S17 HR XPS spectrum of C 1s.

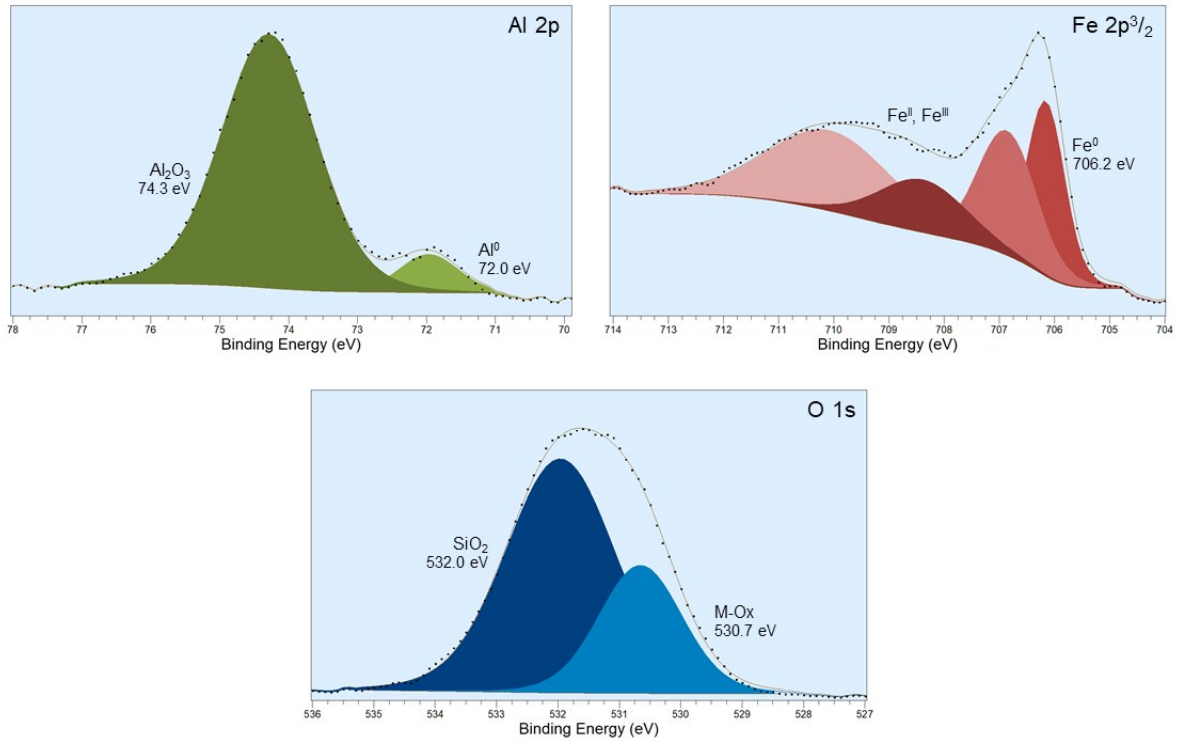

Fig. S18 XPS of the co-sputtered Fe/Al on the silicon wafer. Top: HR-spectra of Al 2p and Fe 2p $^{3}/_{2}$, bottom: HR-spectrum of O 1s.

Analysis of co-sputtered Fe/Al in [BMIm][NTf$_2$]

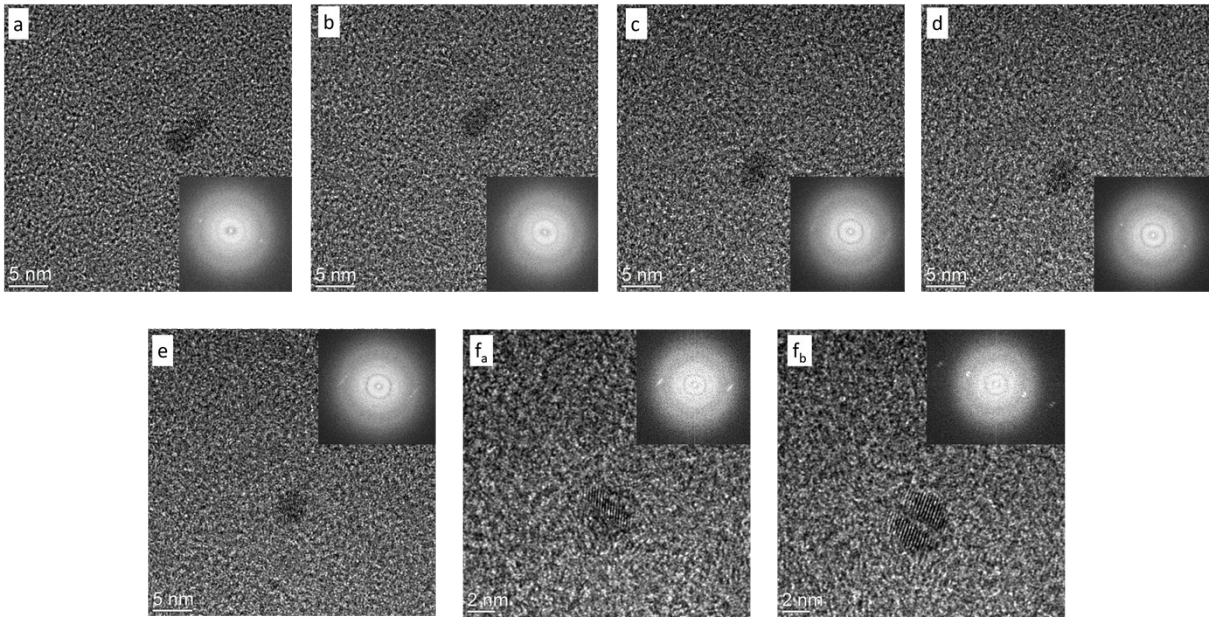

Fig. S19 TEM images of the co-sputtered Fe/Al nanoparticles in [BMIm][NTf$_2$] a) t = 0 min, b) t = 5 min, c) t = 10 min d) t = 12 min and e/f) t = 15 min

The samples in [BMIm][NTf$_2$] show a large amount of material, which is only partly crystalline. There are individual crystalline nanoparticles to recognize. Under the influence of the energy of the electron beam, (amorphous) particles are induced to (re-)crystallize and adjacent

particles are induced to merge over time (Fig. S19). In Fig. S19a two individual particles are visible, which have merged (grown together) after 5 min (Fig. S19b). Depending on the focal plane, different lattice planes can be recognized in the coalesced particle (Fig. S19f_a and f_b).

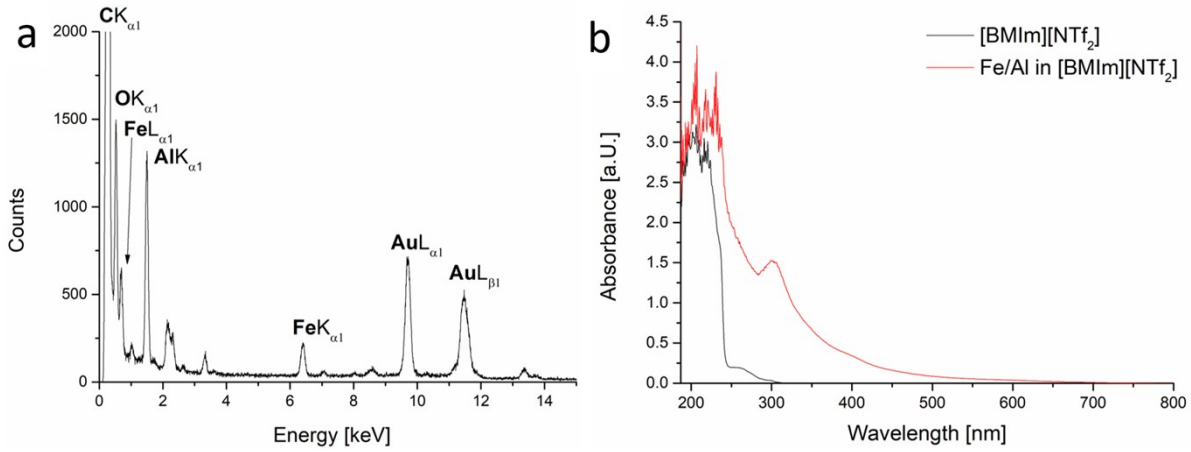

Fig. S20 (a) EDX of the co-sputtered Fe/Al nanoparticles in [BMIm][NTf_2]. (b) UV/VIS spectrum of the co-sputtered Fe/Al nanoparticles in [BMIm][NTf_2].

The co-sputtered Fe/Al sample was also heated for 2 h and 5 h at 100 °C (Fig. S21 and Fig. S22).

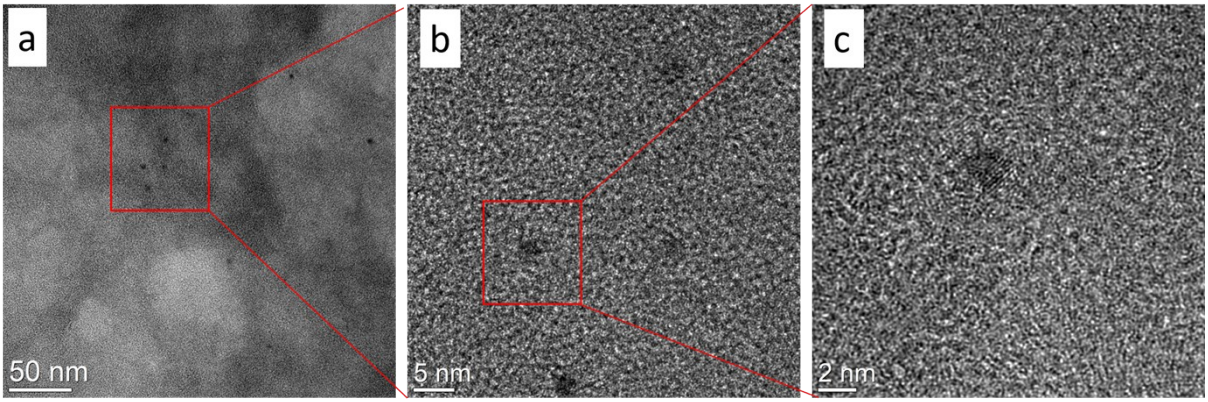

Fig. S21 (a-c) TEM images of the heated sample of the co-sputtered Fe/Al nanoparticles in [BMIm][NTf_2] after 2 h.

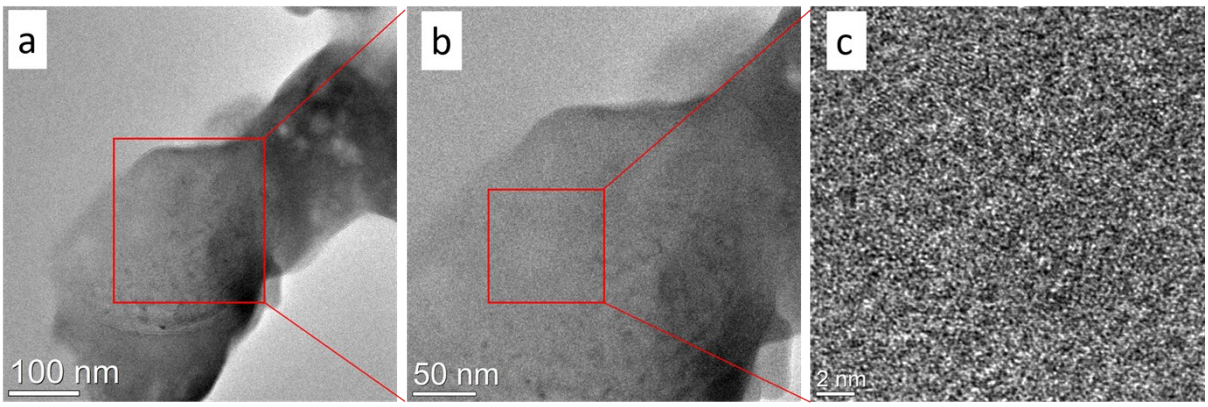

Fig. S22 (a-c) TEM images of the heated sample of the co-sputtered Fe/Al nanoparticles in [BMIm][NTf_2] after 5 h.

Analysis of co-sputtered Fe/Al in [BPy][NTf$_2$]

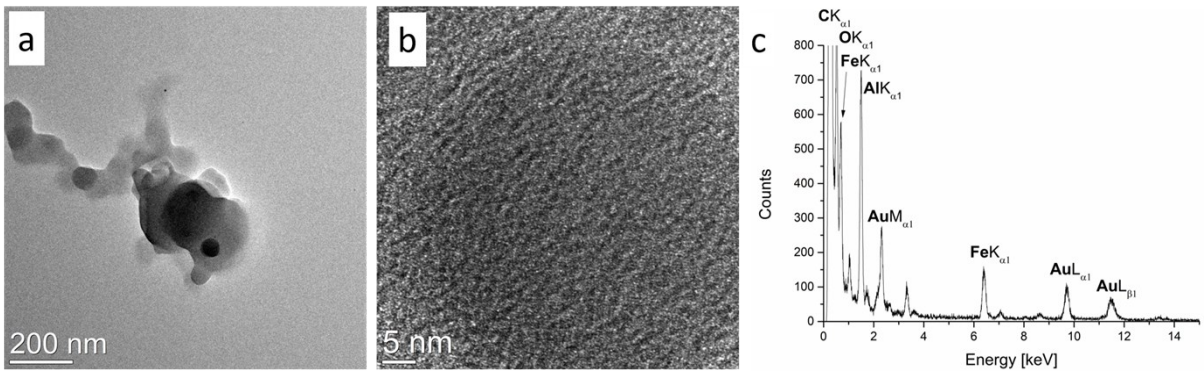

Fig. S23 (a,b) TEM-Images of the particles of the co-sputtered Fe/Al nanoparticles in [BPy][NTf$_2$]. (c) EDX spectrum.

The TEM images showed that there is little material in the sample. This can be attributed to the observed unstable dispersion of the material in the IL. The material precipitated directly after the synthesis. The sample showed accumulations of material which are not crystalline and occasionally particles which are crystalline (Fig. S23). The EDX of the sample demonstrated that there is more aluminium in the sample than iron.

Annealing of co-sputtered Fe/Al in [OPy][NTf$_2$]

In order to promote the crystallization of the NPs outside of the TEM, the Fe/Al@[OPy][NTf$_2$] sample was at first heated (annealed) for 2 h at 100 °C in vacuum. The TEM images of the annealed Fe/Al@[OPy][NTf$_2$] sample in Fig. S24 show that the NPs become more crystalline upon annealing. Still, only a low number of crystalline NPs could be found. The EDX spectrum (Fig. S24c) shows the remains of adhering IL with the sulfur signal originating from the IL anion. The Fe:Al molar ratio of 20:80 at.% did not change with annealing.

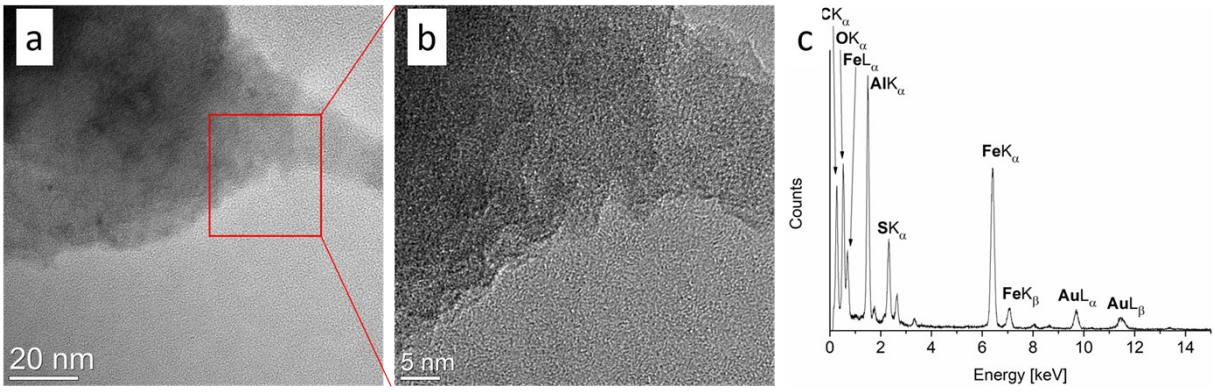

Fig. S24 (a, b) TEM-Images of the co-sputtered Fe/Al NPs in [OPy][NTf2] after annealing for 2 h at 100 °C (c) EDX spectrum of the image region. The Au and C signals in the EDX are caused by the TEM grid.

In order to continue the crystallization, the sample was heated three more hours in vacuum. TEM images after annealing for then altogether 5 h are shown in Fig. S25.

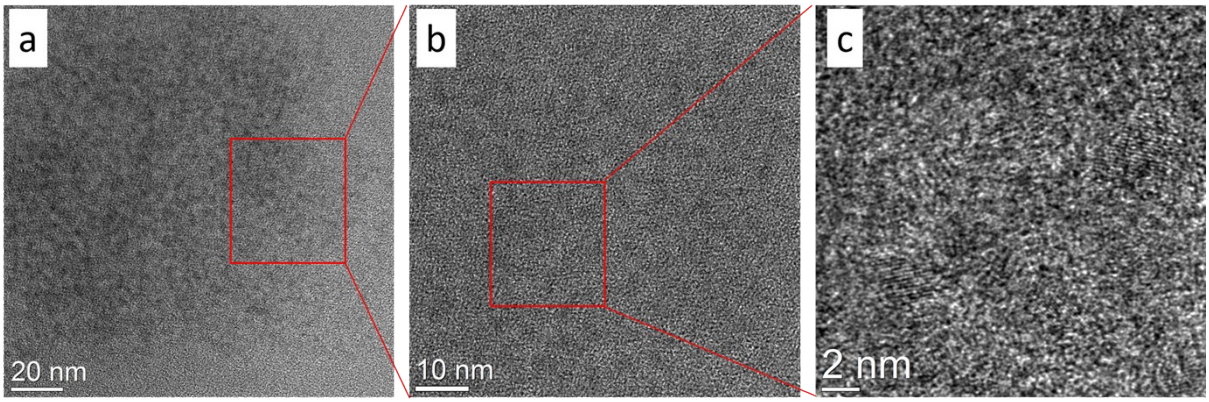

Fig. S25 TEM-Images of the Fe/Al NPs sputtered in [OPy][NTf2] after annealing for altogether 5 h at 100 °C.

Even though more crystalline particles could be found, it was still not possible to measure a diffraction pattern because of the small size of the nanoparticles. A measured fast Fourier transform (FFT) analysis gave only two reflexes so that a phase analysis was not possible. The sample was heated again for another 5 h at 100 °C, then prepared for the TEM measurement so that more crystalline particles should be found. After a total annealing time of 10 h, embedded Fe/Al nanoaggregates in the ionic liquid matrix (Fig. 5a,b, main text) FFT analysis of the HR-TEM images (Fig. 5e, main text) gave a clear indication of a Fe_4Al_{13} phase (see main text).

Fig. S26a shows another area where dark spots of Fe/Al NPs are observed at a size of about 2-3 nm in diameter. The enlargement of Fig. S26b gives only a weak indication of existing crystal lattices, thus, FFT filtering was applied. Also, in the filtered image the lattice is hardly visualized and appears full of defects (Fig. S26c). Nevertheless, in the FFT image the lattice spacings typical for Fe_4Al_{13} could be identified (Fig. S26d). Additionally, massive patches of the ionic liquid were detected, see *e.g.* Fig. S27a,b. The filtered high-resolution image (Fig. S27c) reveals a nicely crystallized 10 nm large nanoparticle composed of Fe_4Al_{13} as evidenced by the analysis of the FFT image (Fig. S27d).

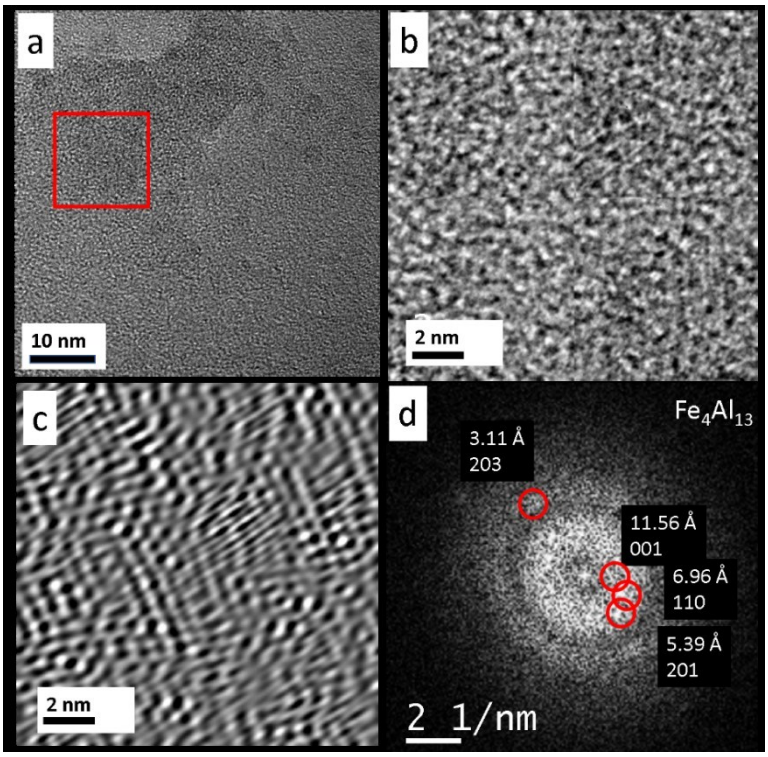

Fig. S26 (a) TEM image of co-sputtered Fe/Al NPs embedded in the IL [OPy][NTf_2]. (b) High-resolution of red frame area in (a) displays NPs, which are hardly discernible. (c) FFT filtered image of (b) reveals poor crystal lattice with indications for the positions of the NPs (d) Fast Fourier transform (FFT) of (b) with marked reflections of Fe_4Al_{13}.

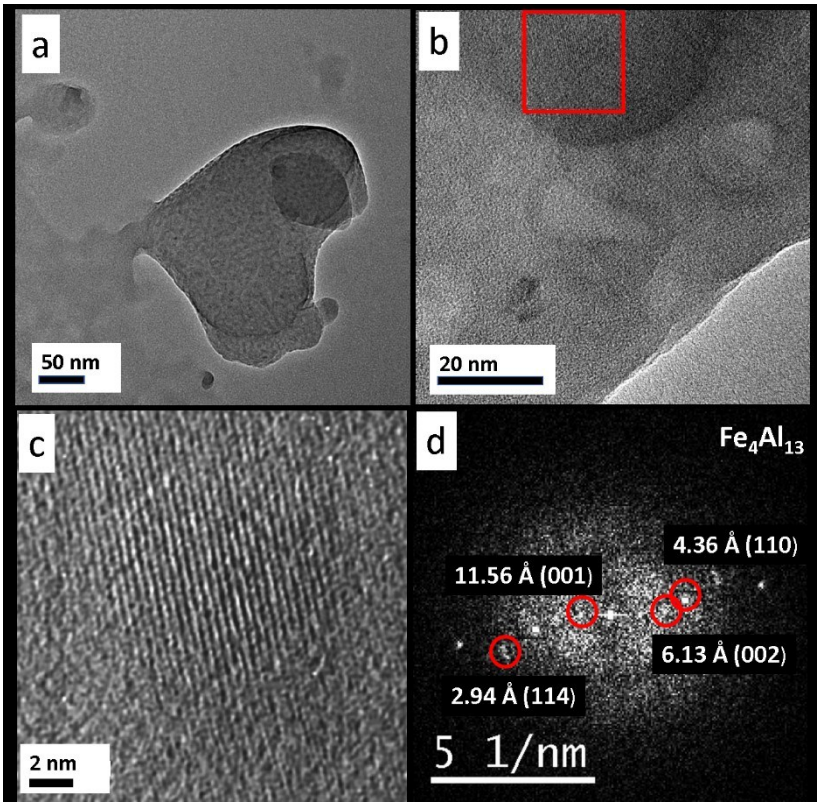

Fig. S27 (a) TEM image of a patch of the IL ([OPy][NTf_2]) matrix. (b) Zoomed area of (a). (c) Amorphous background filtered high-resolution image of red frame area in (b) reveals crystal lattices within an Fe/Al nanoparticle. (d) FFT of (c) with marked reflections of Fe_4Al_{13}.

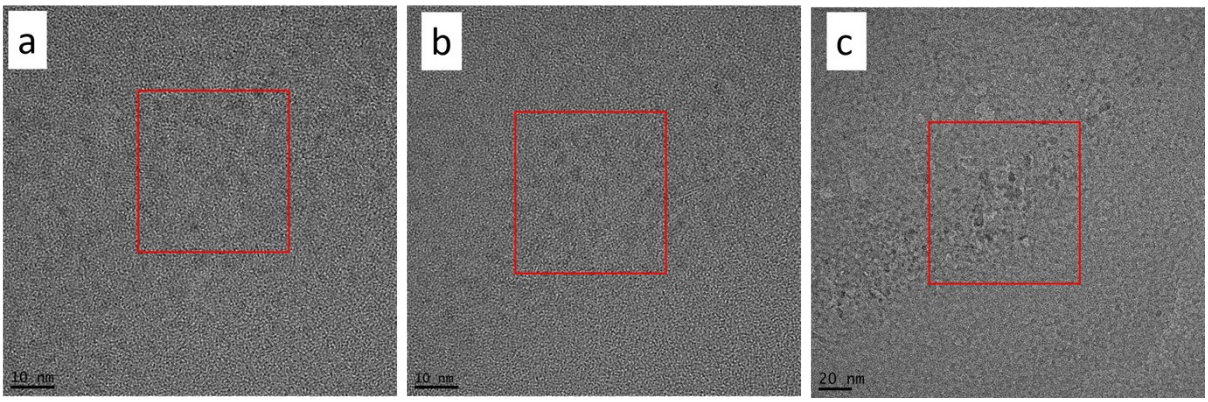

Fig. S28 TEM images of the co-sputtered Fe/Al nanoparticles in [OPy][NTf_2] after 10 h heating at 100 °C followed by the in-situ crystallization process through the electron beam in the TEM at 300 kV and a magnification of 490 kx. Every 10 minutes a picture was taken: (a) 0 min; (b) 10 min; (c) 20 min.

1 L. H. J. Lajunen and P. Peramaki, in Spectrochemical Analysis by Atomic Absorption and Emission, Royal Society of Chemistry, Cambridge, 2004, pp. 142-144.

2 G. Beamson and D. Briggs, *High Resolution XPS of Organic Polymers – The Scienta ESCA300 Database Wiley Interscience*, Chichester, 1992.

3 M. C. Biesinger, B. P. Payne, A. P. Grosvenor, L. W. M. Lau, A. R. Gerson and R. St. C. Smart, *Appl. Surf. Science*, 2011, **257**, 2717-2730.